Supporting Information

Layerwise Replacement Method to Achieve High Solar-to-Hydrogen efficiency for Photocatalytic Water Splitting: A First Principles Study

Chuye Quan,[a,b] Shilei Ji,[a] Ruijia Yao,[a] Ming Du,[a] Chen Chen,[c] Xiaoyang He,[c] Ran Cai,[d] Jianping Yang[c] and Xing'ao Li [a,c]

[a] Institute ofAdvanced Materials *(IAM)*, Nanjing University of Posts & Telecommunications *(NJUPT)*, Nanjing 210023, China
[b] Tongda College, Nanjing University of Posts and Telecommunications, Yangzhou 225100, China
[c] School of Science, Jiangsu Provincial Engineering Research Center of Low Dimensional Physics and New Energy, Nanjing University of Posts and Telecommunications (NJUPT), Nanjing 210023, China
[d] School of Medical Technology, Beijing Institute of Technology

Computational details

DFT-1/2 is based on Slater's half-occupation technique, with the -1/2 denoting an intermediate position between the initial ground state and the ionized state.[1-2] The DFT-1/2 method introduces the computed atomic self-energy potential into solids, where it is incorporated into the pseudopotential as a common pseudopotential for calculating electronic structures.[3-4] The self-energy potential requires correction before its introduction. The self-energy potential's reach is primarily constrained by the cutoff radius r_{cut}. The potential is trimmed by a function as

$$\Theta = \begin{cases} \left[1 - \left(\frac{r}{CUT}\right)^n\right]^3, r \le CUT \\ 0 \qquad\qquad , r > CUT \end{cases} \qquad \text{S(1)}$$

Since r_{cut} is variable, selecting an appropriate value for r_{cut} results in the maximum presentation of the bandgap, where the correction is maximized. In this work, we determine the appropriate r_{cut} for the atoms through testing. We set the parameter n to 8, a value also used in other articles.

The formation energy of all the structures are evaluated by the following formula:

$$E_f = \frac{E_{total} - \sum_i n_i \mu_i}{\sum_i n_i} \qquad \text{S (2)}$$

where E_{total} and n_i represent the total energy and the number of i-th atom of the structures in a unit cell, and μ_i is the cohesive energy of the i-th atom in its bulk crystal.

The calculation formula of plane-averaged charge density differences $\Delta\rho_{(z)}$ is as follow:

$$\Delta\rho_{(z)} = \rho_{Al_2S_2Se-t} - \rho_{Al} - \rho_S - \rho_{Se} \qquad \text{S (3)}$$

$$\Delta\rho_{(z)} = \rho_{Al_2TeSe_2-t} - \rho_{Al} - \rho_{Te} - \rho_{Se} \qquad \text{S (4)}$$

The formula for calculating the photoabsorption coefficient (α_ω), denoted as (S5), incorporates the frequency (ω), with $\varepsilon'(\omega)$ and $\varepsilon''(\omega)$ representing the real and imaginary parts of the dielectric function, respectively. These parameters were obtained using the HSE06 hybrid functional.

$$\alpha_{\omega} = \frac{\sqrt{2}\omega}{2}\left[\sqrt{\left(\varepsilon^{'}(\omega)\right)^2 + \left(\varepsilon^{''}(\omega)\right)^2} - \varepsilon^{'}(\omega)\right]^{1/2} \quad \text{S (5)}$$

The Gibbs free energy change (△G) in the water redox reactions is defined as:

$$\Delta G = \Delta E + \Delta E_{ZPE} - T\Delta S \quad \text{S (6)}$$

where ΔE, ΔE_{ZPE}, and ΔS represent the energy difference of adsorption, zero-point energy and entropy, respectively. T is system temperature (298 K).

The OWS process comprises two half-reactions: HER, which involves a two-electron reaction, and OER, which is a four-electron reaction in an acidic solution. The OER process can be written as:

Step 1: $* + H_2O \longrightarrow *OH + e^- + H^+$ S (7)

Step 2: $*OH \longrightarrow *O + e^- + H^+$ S (8)

Step 3: $*O + H_2O \longrightarrow *OOH + e^- + H^+$ S (9)

Step 4: $*OOH \longrightarrow O_2 + e^- + H^+$ S (10)

The HER process can be described as:

Step 1: $* + H^+ + e^- \longrightarrow *H$ S (11)

Step 2: $*H + H^+ + e^- \longrightarrow H_2$ S (12)

Then, the △G for OER are achieved as:

Step 1: $\Delta G = G_{*OH} + \frac{1}{2}G_{H_2} - G_{H_2O} - G_{*} - U_h$ S (13)

Step 2: $\Delta G = G_{*O} + \frac{1}{2}G_{H_2} - G_{*OH} - U_h$ S (14)

Step 3: $$\Delta G = G_{*OOH} + \frac{1}{2}G_{H_2} - G_{H_2O} - G_{*O} - U_h$$ S (15)

Step 4: $$\Delta G = G_{*} + \frac{1}{2}G_{H_2} + G_{*O} - G_{*OOH} - U_h$$ S (16)

The △G for HER is calculated by:

$$\Delta G = G_{*H} - \frac{1}{2}G_{H_2} - G_{*} - U_e$$ S (17)

the μ_α of 2D materials can be expressed as the following equation: [5-6]

$$\mu_\alpha = \frac{e\hbar^3 C_\alpha}{k_B T \left|m_\alpha^*\right| m_d \left(E_\alpha^l\right)^2}$$ S (18)

$$C_\alpha = \frac{2}{S_0}\frac{\partial^2 E_{total}}{\partial(\Delta l_\alpha / l_\alpha^0)^2}$$ S (19)

$$E_\alpha^l = \frac{\Delta E_{ks}}{\Delta l_\alpha / l_\alpha^0}$$ S (20)

Here, e denotes the electron charge, $\hbar$ represents the reduced Planck constant, k_B stands for the Boltzmann constant, T denotes the temperature (set to T = 300K), m_α^* corresponds to the effective mass in the α direction of the material without strain (where α is either the x or y direction), m_d is the average effective mass ($m_d = \sqrt{m_x^* m_y^*}$). C_α denotes the elastic modulus, with S_0 represents the area of the optimized 2D unit cell without strain, E_{total} represents the total energy of the system, l_α^0 corresponds to the lattice constant without strain, and Δl_α signifies the change in lattice constant. The deformation potential is calculated as S (18).

Other supplementary contents

The HSE06 Hybrid functionals typically yield more accurate bandgaps, but their computational demands are higher.[1] The DFT-1/2 method, introduced in recent years as a correction function for DFT, mitigates the problem of underestimated bandgaps in standard DFT by rectifying the self-energy of valence band holes, all while maintaining rapid computational speed. [3, 7] Previously, DFT-1/2 has successfully predicted the bandgaps of various semiconductor materials, ranging from metal oxides to halide perovskites, with accuracy comparable to GW but at lower computational cost.[8] In this work, the computational results indicate that, except for Al_2S_2Te-t and Al_2TeS_2-m, the E_g of other materials calculated with PBE are approximately 0.8 eV smaller than those obtained with HSE06, while the difference between the HSE06 band gap and the DFT-1/2 corrected E_g is around 0.2 eV. Considering the fast computation speed and extremely low cost of the DFT-1/2 method, for large systems with similar structures, we can use the DFT-1/2 method to evaluate the E_g. The significant difference in E_g predicted for Al_2S_2Te-t and Al_2TeS_2-m monolayers using the HSE06 and DFT-1/2 methods may be due to their metallic nature as predicted by PBE.

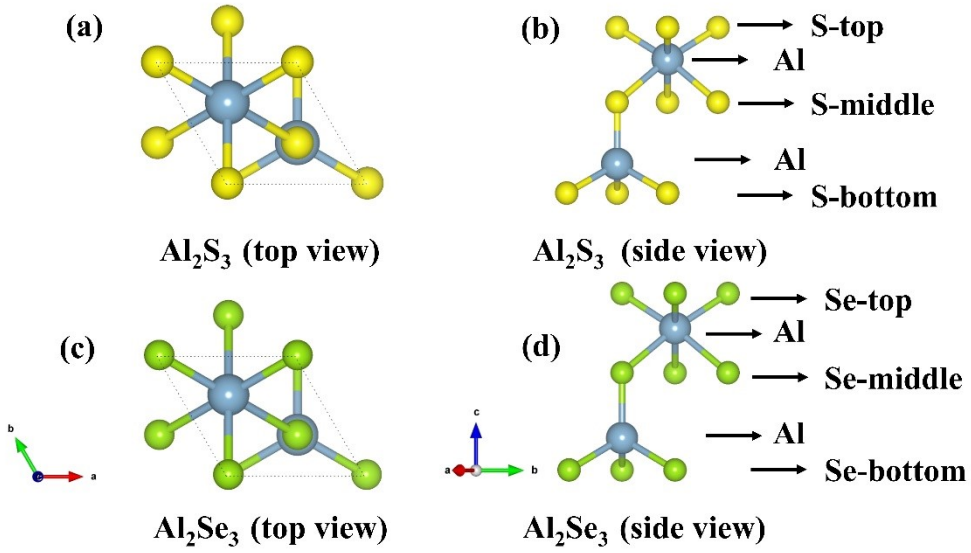

Fig. S1. The unit cells of Al_2S_3 and Al_2Se_3 monolayers.

Tab. S1. The lattice constant (a), formation energy (E_f), band gap (E_g), and electrostatic potential difference ($\Delta\Phi$) of other 10 types of Al_2X_2X' monolayers except for Al_2S_2Se-t and Al_2TeSe_2-m.

	a(Å)	E_f (eV/atom)	E_g (eV)/ PBE	E_g (eV)/ DFT-1/2	E_g (eV)/ HSE06	ΔΦ
Al_2S_2Te-t	3.750	-0.896	—	0.211	1.195	0.165
Al_2TeS_2-m	3.70	-0.841	—	0.829	0.403	1.892
Al_2S_2Te-b	3.774	-0.864	1.791	2.415	2.465	2.285
Al_2S_2Se-t	3.638	-1.108	1.154	2.091	1.839	2.230
Al_2SeS_2-m	3.618	-1.084	1.427	2.178	2.202	2.202
Al_2S_2Se-b	3.640	-1.096	2.431	3.360	3.255	2.287
Al_2Se_2S-t	3.692	-1.009	1.813	2.653	2.575	2.123
Al_2SSe_2-m	3.716	-1.035	1.679	2.595	2.361	2.109
Al_2Se_2S-b	3.691	-1.020	1.237	2.219	1.973	2.075
Al_2Se_2Te-t	3.891	-0.795	0.253	1.050	0.807	1.584
Al_2TeSe_2-m	3.854	-0.762	0.522	1.323	1.157	1.714
Al2Se2Te-b	3.900	-0.779	1.959	2.377	2.728	1.999

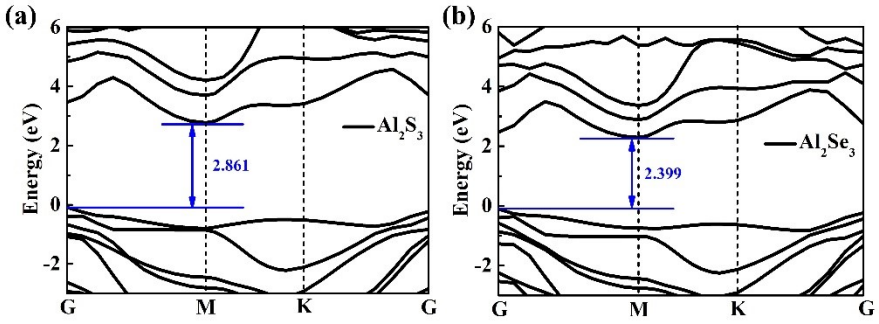

Fig. S2. The electronic band structures of Al_2S_3 and Al_2Se_3 monolayers at the HSE06 level.

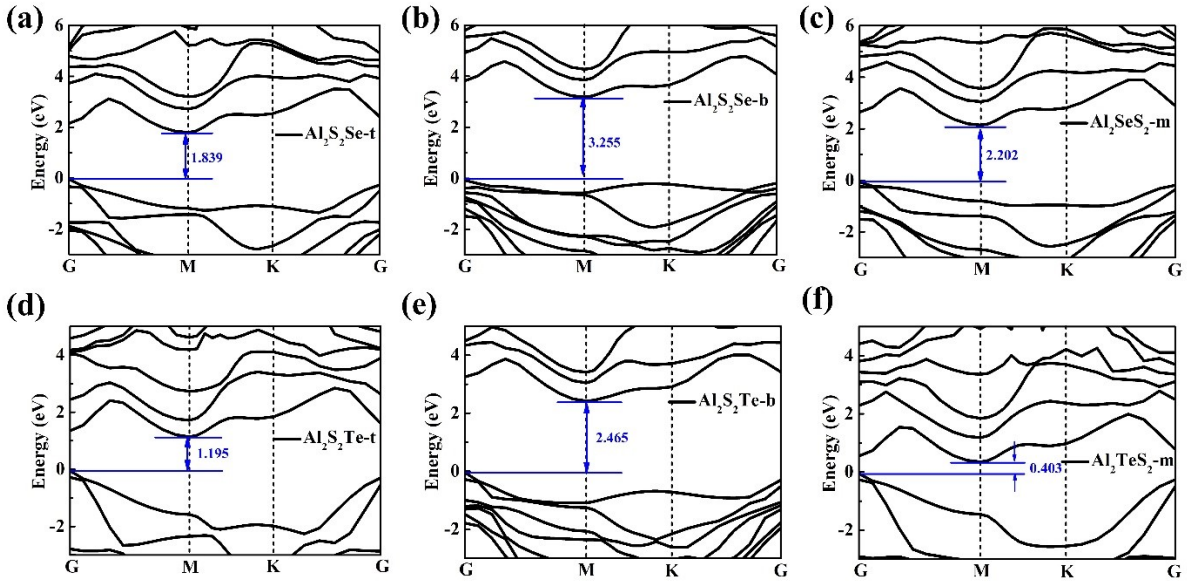

Fig. S3 (a-f). The electronic band structures of Al_2S_2Se-t, Al_2S_2Se-b, Al_2SeS_2-m, Al_2S_2Te-t, Al_2S_2Te-b and Al_2TeS_2-m monolayers at the HSE06 level.

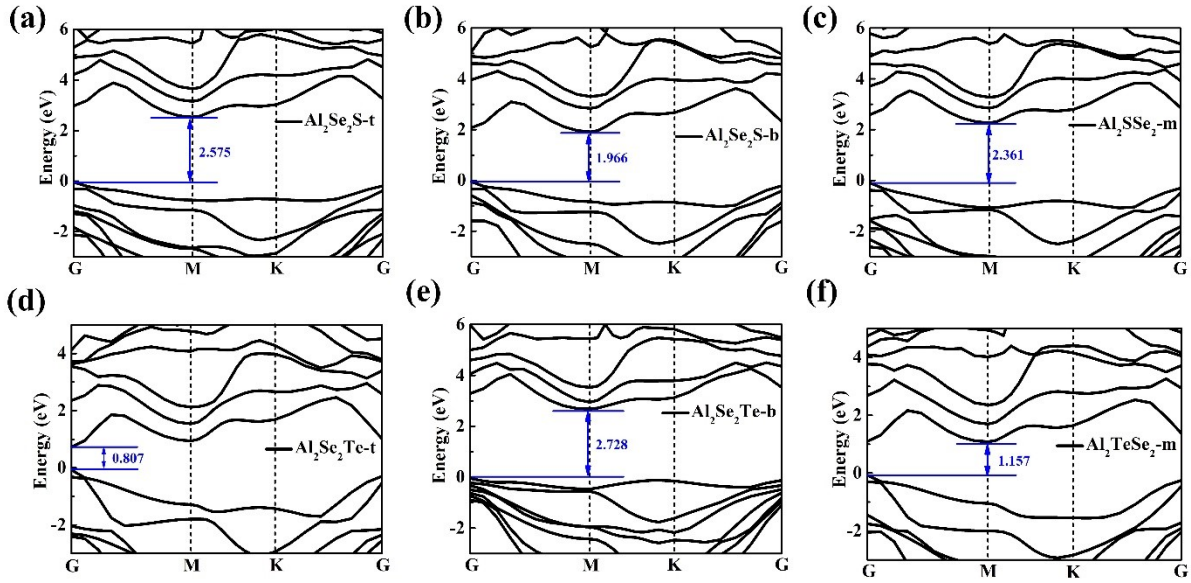

Fig. S4 (a-f). The electronic band structures of Al_2Se_2S-t, Al_2Se_2S-b, Al_2SSe_2-m, Al_2Se_2Te-t, Al_2Se_2Te-b and Al_2TeSe_2-m monolayers at the HSE06 level.

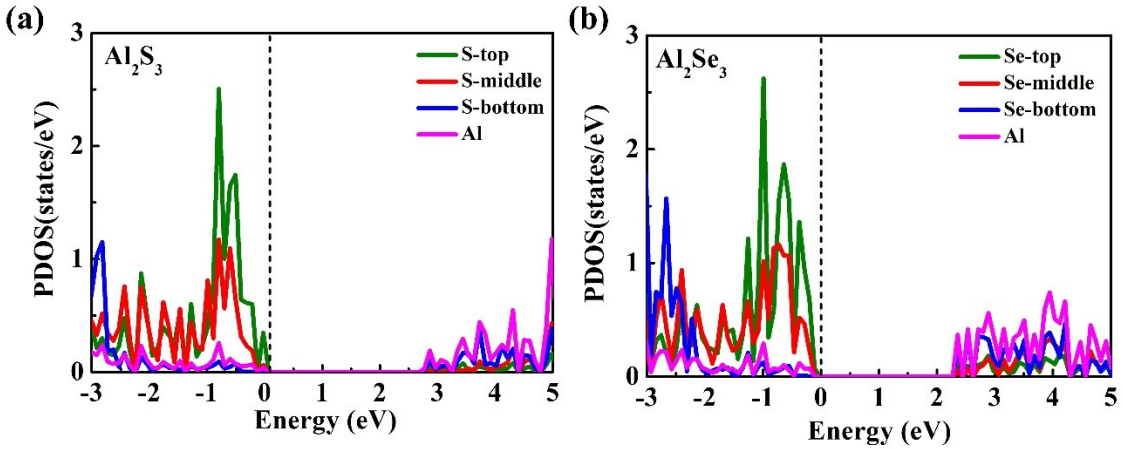

Fig. S5 (a-b) The PDOS of Al_2S_3 and Al_2Se_3 monolayers at the HSE06 level

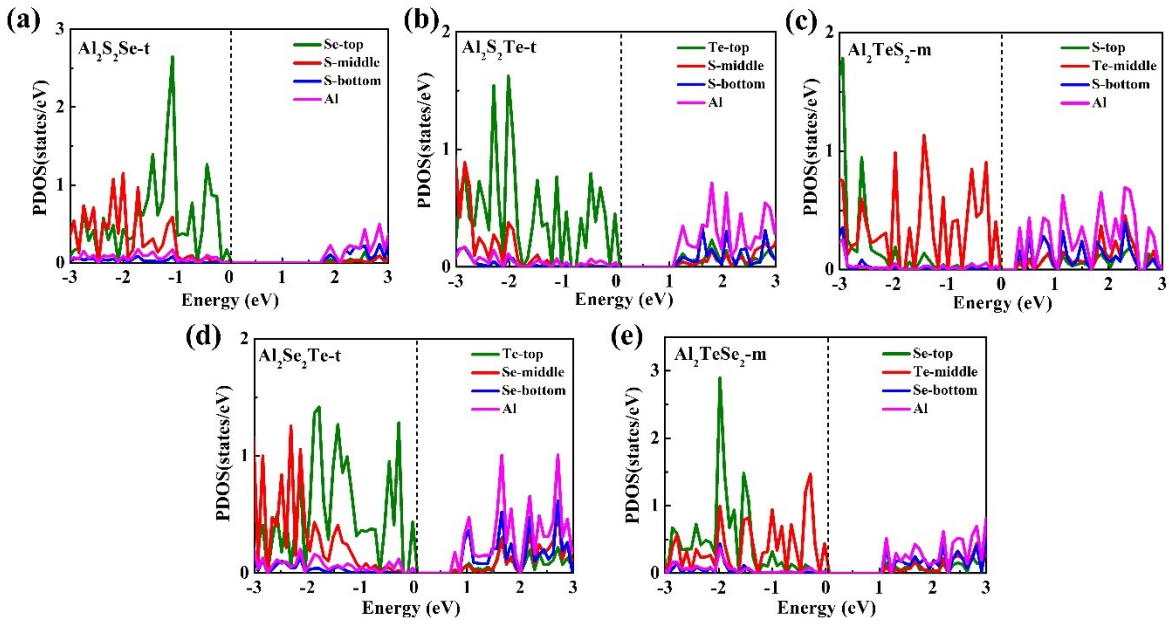

Fig. S6 (a-e) The PDOS of Al_2S_2Se-t, Al_2S_2Te-t, Al_2TeS_2-m, Al_2Se_2Te-t and Al_2TeSe_2-m monolayers at the HSE06 level.

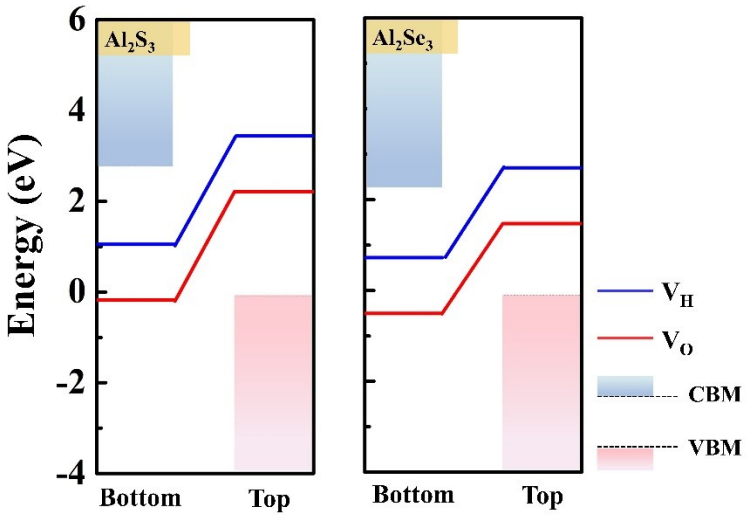

Fig. S7. The band alignment relative to the water redox potentials for Al_2S_3 and Al_2Se_3 monolayers.

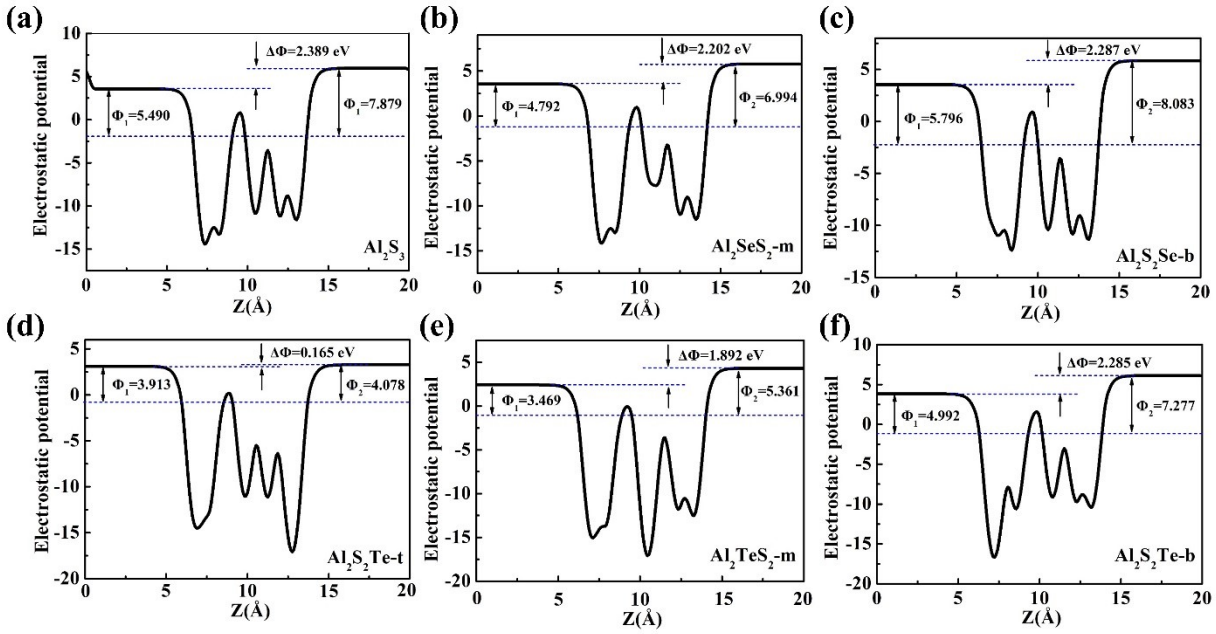

Fig. S8. The electrostatic potentials, Fermi level and work functions of Al_2S_3, Al_2SeS_2-m, Al_2S_2Se-b, Al_2S_2Te-t, Al_2TeS_2-m and Al_2S_2Te-b monolayers along the Z-direction.

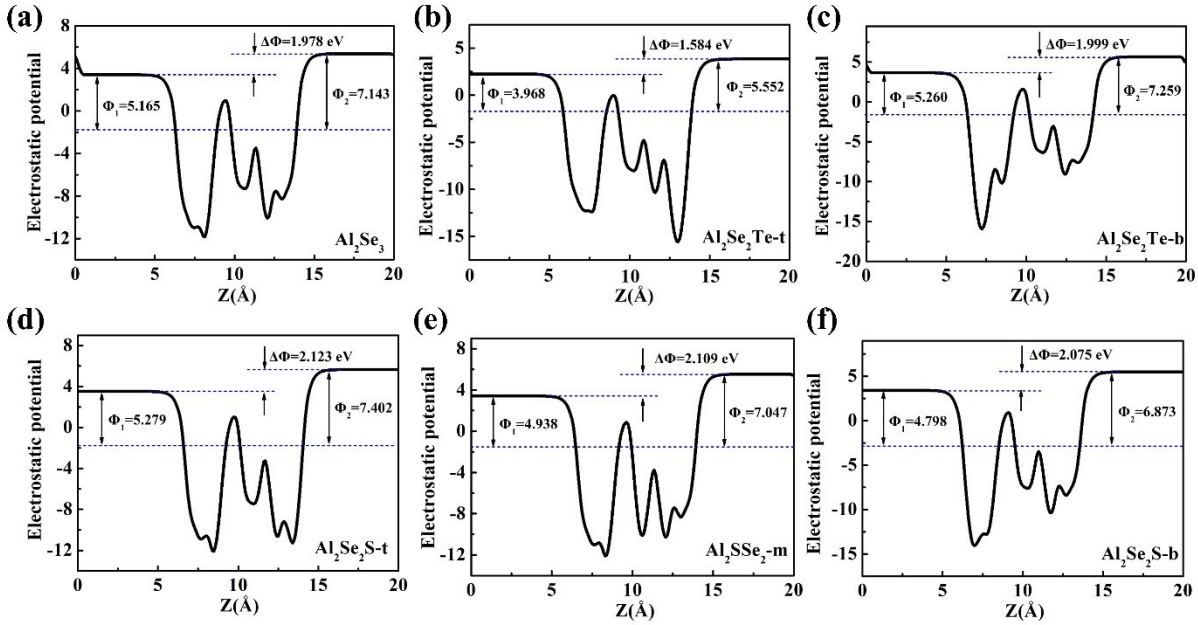

Fig. S9. The electrostatic potentials, Fermi level and work functions of Al_2Se_3, Al_2Se_2Te-t, Al_2Se_2Te-b, Al_2Se_2S-t, Al_2SSe_2-m and Al_2Se_2S-b monolayers along the Z-direction.

Table S2. The overpotentials $\chi(H_2)$ and $\chi(O_2)$, energy conversion efficiency of light absorption (η_{abs}), carrier utilization efficiency (η_{cu}), STH efficiency (η_{STH}), and corrected STH ($\eta_{STH}^{'}$).

	χ_{H_2}	χ_{O_2}	η_{abs}	η_{cu}	η_{STH}	$\eta_{STH}^{'}$
Al_2S_3	**1.723**	**2.297**	**8.5%**	**38.5%**	**3.3%**	**3.1%**
Al_2Se_3	**1.570**	**1.577**	**21.0%**	**43.6%**	**9.2%**	**8.0%**
Al_2S_2Te-t	**1.668**	**-1.538**	**76.6%**	**1.2%**	**0.9%**	**0.9%**
Al_2TeS_2-m	**1.320**	**-0.255**	**99.3%**	**46.0%**	**45.7%**	**20.2%**
Al_2S_2Te-b	**1.870**	**1.650**	**18.9%**	**42.9%**	**8.1%**	**7.0%**
Al_2S_2Se-t	**1.664**	**1.176**	**44.2%**	**51.6%**	**22.8%**	**16.1%**
Al_2SeS_2-m	**1.729**	**1.382**	**28.2%**	**46.2%**	**13.0%**	**10.5%**
Al_2S_2Se-b	**1.827**	**2.484**	**3.3%**	**35.0%**	**1.1%**	**1.1%**
Al_2Se_2S-t	**1.691**	**1.777**	**15.6%**	**41.6%**	**6.5%**	**5.9%**
Al_2SSe_2-m	**1.765**	**1.474**	**22.4%**	**44.1%**	**9.9%**	**8.4%**
Al_2Se_2S-b	**1.553**	**1.254**	**38.0%**	**49.5%**	**18.8%**	**14.3%**
Al_2Se_2Te-t	**1.199**	**-0.038**	**90.7%**	**42.1%**	**38.2%**	**20.6%**
Al_2TeSe_2-m	**1.305**	**0.336**	**78.8%**	**49.9%**	**39.3%**	**25.9%**
Al_2Se_2Te-b	**1.865**	**1.632**	**11.4%**	**39.9%**	**4.5%**	**4.3%**

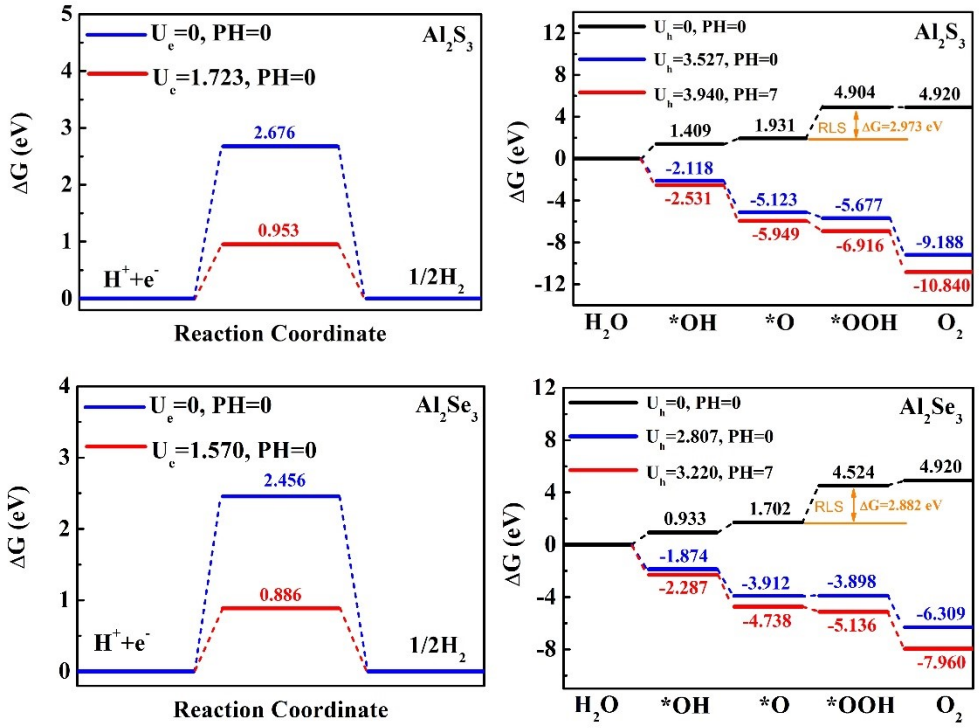

Fig. S10. The Gibbs free energy change diagrams for the OER and HER on the Al_2S_3 and Al_2Se_3 monolayers.

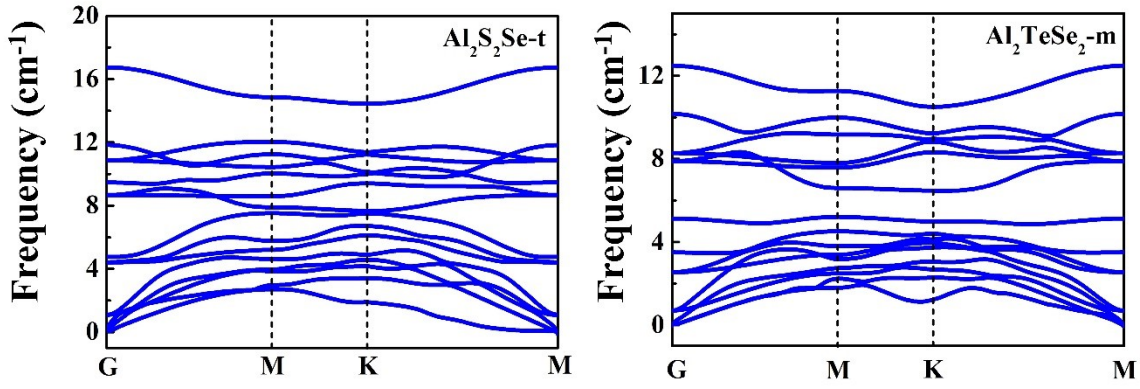

Fig. S11. Phonon band structure of Al_2S_2Se-t and Al_2TeSe_2-m monolayers.

Tab. 2. Effective mass m_α^*, elastic modulus C_α, deformation potential E_α^l, and carrier mobility μ_α of Al_2S_2Te-b, Al_2SeS_2-m, Al_2S_2Se-b, Al_2Se_2S-t, Al_2SSe_2-m, Al_2Se_2S-b, Al_2Se_2Te-t and Al_2Se_2Te-b mnolayers.

Material	Direction	$m_\alpha^*(m_e)$		E_α^l (eV)		C_α (J/m²)	μ_α (cm²/(s*V))	
		e	h	e	h	h=e	e	h
Al_2S_2Te-b	**x**	**0.61**	**0.73**	**2.50**	**11.45**	**161.43**	**1415.96**	**50.90**

	y	**0.65**	**0.68**	**3.09**	**11.98**	**176.17**	**951.44**	**54.09**
Al_2SeS_2-m	**x**	**0.62**	**6.44**	**3.69**	**8.99**	**232.21**	**1200.39**	**3.28**
	y	**0.38**	**1.31**	**6.63**	**9.92**	**241.97**	**625.72**	**13.79**
Al_2S_2Se-b	**x**	**0.66**	**2.20**	**3.21**	**6.30**	**210.00**	**1123.81**	**18.24**
	y	**0.51**	**3.59**	**5.73**	**7.45**	**223.97**	**493.91**	**8.53**
Al_2Se_2S-t	**x**	**0.62**	**8.49**	**3.78**	**8.23**	**212.34**	**1054.75**	**1.57**
	y	**0.37**	**2.95**	**6.14**	**9.46**	**222.30**	**694.38**	**3.59**
Al_2SSe_2-m	**x**	**0.63**	**2.32**	**3.92**	**10.12**	**190.54**	**849.83**	**9.98**
	y	**0.38**	**1.26**	**6.76**	**10.75**	**206.41**	**513.74**	**17.74**
Al_2Se_2S-b	**x**	**1.05**	**1.60**	**3.81**	**8.38**	**215.23**	**327.41**	**11.98**
	y	**0.81**	**7.26**	**7.01**	**10.63**	**225.58**	**130.85**	**1.72**
Al_2Se_2Te-t	**x**	**0.78**	**1.48**	**10.53**	**11.72**	**179.12**	**76.88**	**17.25**
	y	**0.42**	**0.80**	**11.42**	**12.37**	**190.85**	**130.43**	**30.50**
Al_2Se_2Te-b	**x**	**1.10**	**2.64**	**3.44**	**5.50**	**189.11**	**186.41**	**19.21**
	y	**2.52**	**2.60**	**5.69**	**7.82**	**202.25**	**31.80**	**10.33**

References

(1) Ferreira, L. G.; Marques, M.; Teles, L. K. Slater Half-occupation Technique Revisited: the LDA-1/2 and GGA-1/2 Approaches for Atomic Ionization Energies and Band Gaps in Semiconductors. *AIP Adv.* **2011,** *1*, 0321191-03211911.

(2) Yao, R.; Ji, S.; Zhou, T.; Quan, C.; Liu, W.; Li, X. Self-energy Correction and Numerical Simulation for Efficient Lead-free Double Perovskite Solar Cells. *Phys. Chem. Chem. Phys.* **2024,** *26*, 5253-5261.

(3) Ferreira, L. G.; Marques, M.; Teles, L. K. Approximation to Density Functional Theory for The Calculation of Band Gaps of Semiconductors. *Phys. Rev. B* **2008,** *78*, 125116.

(4) Traore, B.; Even, J.; Pedesseau, L.; Képénekian, M.; Katan, C. Band gap, effective masses, and energy level alignment of 2D and 3D halide perovskites and heterostructures using DFT-1/2. *Phys. Rev. Mater.* **2022,** *6*, 014604.

(5) Li, X.; Dai, Y.; Li, M.; Wei, W.; Huang, B. Stable Si-based Pentagonal Monolayers: High Carrier Mobilities and Applications in Photocatalytic Water Splitting. *J. Mater. Chem. A* **2015,** *3*, 24055-24063.

(6) Cai, Y.; Zhang, G.; Zhang, Y. W. Polarity-reversed Robust Carrier Mobility in Monolayer MoS_2 Nanoribbons. *J. Am. Chem. Soc.* **2014,** *136*, 6269-6275.

(7) Xue, K.-H.; Yuan, J.-H.; Fonseca, L. R. C.; Miao, X.-S. Improved LDA-1/2 method for band structure calculations in covalent semiconductors. *Comp. Mater. Sci.* **2018,** *153*, 493-505.

(8) Guilhon, I.; Koda, D. S.; Ferreira, L. G.; Marques, M.; Teles, L. K. Approximate Quasiparticle Correction for Calculations of the Energy Gap in Two-dimensional Materials. *Phys. Rev. B* **2018,** *97*, 045426.